ROYAL SOCIETY
OF CHEMISTRY

EDGE ARTICLE

Check for updates

All publication charges for this article have been paid for by the Royal Society of Chemistry

Water-accelerated photooxidation and degradation of lignin linkages mediated by plasmonic catalysts†

Juhee Ha, [iD] ‡[a] Jiwon Kang,‡[a] Suk Hyun Lim,[a] Dae Won Cho, [iD] [a] Kwang-Im Oh [iD] *[b] and Youngsoo Kim [iD] *[a]

The selective oxidation and degradation of lignin are crucial for realizing its potential as a biofuel or petroleum substitute. Despite the importance of C–C bond cleavage for lignin valorization, this process is significantly challenging. Herein, we present plasmonic gold nanoparticles (Au NPs) as environmentally friendly and reusable photocatalysts for the chemoselective oxidation of the benzylic hydroxyl groups of lignin and subsequent lignin degradation. The oxidation process is driven by the generation of superoxide ions ($O_2^{\bullet-}$), leading to proton release and initiating lignin photooxidation through a mechanism termed plasmon-driven hydrogen atom abstraction and degradation (p-HAADe). Our results demonstrate the significant suppression of lignin oxidation and degradation in acetonitrile-rich environments, while aqueous conditions notably enhance these processes. Furthermore, two distinct time-dependent regimes are identified, namely, the "oxidation dominant" regime, where lignin oxidation is predominant, and the "degradation dominant" regime, favoring C_α–C_β bond cleavage. These findings provide crucial insights into optimizing lignin conversion in biofuel applications, highlighting the potential of Au NPs for use in sustainable chemical processes.

Introduction

In conjunction with cellulose and hemicellulose, lignin is a major component of lignocellulose. In recent years, biomass derived from lignocellulose has received growing attention as a renewable energy source with the potential to replace petroleum-based materials.[1–3] Natural lignin is a polymer containing abundant aromatic compounds, and it comprises 15–30 wt% of the lignocellulosic biomass.[4,5] Furthermore, natural lignin consists of both phenolic and non-phenolic structures. The conversion of natural lignin to low-molecular-weight aromatic compounds is of particular interest because of its potential to yield value-added chemical feedstocks through the cleavage of lignin C–O or C–C bonds.[6,7] Previous studies have indicated that the strengths of these bonds in the β-O-4 linkage weakens following hydroxyl group oxidation, rendering it susceptible to cleavage.[5,8–10] For example, computational calculations predicted an approximately 14 kcal mol^{-1} decrease in the C_β–O bond dissociation enthalpy (BDE) of the β-O-4 linkage

upon the oxidation of C_α–OH to C_α=O, thereby facilitating C–O bond cleavage.[8,11] Other studies have revealed that C_α–C_β bond cleavage is possible after the oxidation of the benzylic hydroxyl group.[8,12] However, traditional methods for lignin decomposition, such as pyrolysis, acid–base catalysis, organosolvolysis, krafting, and enzymatic decomposition, have numerous drawbacks, including the requirement for high temperatures, low efficiency, and toxic chemical waste generation.[13–15] Furthermore, these methods, which generally necessitate harsh conditions, tend to exhibit low product selectivity, thereby complicating the extraction of target compounds.[10] To address these challenges, photocatalysis has emerged as a potential technology for lignin decomposition, offering an eco-friendly, highly efficient, and cost-effective process that can be conducted under mild conditions.[16,17] To date, research on the photocatalytic decomposition of lignin has explored various types of catalysts, including organic and metal–organic complexes (homogeneous catalysts), in addition to metal chalcogenides and metal oxides (heterogeneous catalysts).[6,18–20] Plasmonic nanocrystals, particularly single-component Au nanoparticles (NPs), have attracted considerable attention as visible-light-driven photocatalysts owing to their strong light absorption capability in the visible light region and their excellent catalytic activities at the nanoscale.[21–25] Plasmonic Au photocatalysts have been demonstrated to exhibit unique physical behaviors from the perspectives of both kinetics and thermodynamics.[26–28] They have also been shown to drive useful

[a]*Department of Chemistry, Yeungnam University, Gyeongsan, Gyeongbuk 38541, Republic of Korea. E-mail: kimys6553@yu.ac.kr*
[b]*Department of Chemistry, Korea University, Seoul 02841, Republic of Korea. E-mail: orangekwang@gmail.com*

† Electronic supplementary information (ESI) available. See DOI: https://doi.org/10.1039/d4sc08401b
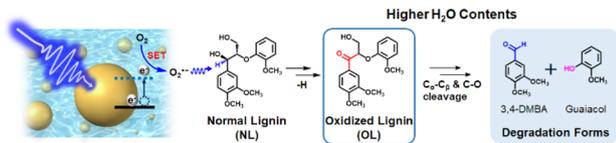
‡ These authors contributed equally.

Fig. 1 Illustration of the stepwise plasmon-driven hydrogen atom abstraction and degradation (p-HAADe) process for the photooxidation of normal lignin (NL) to oxidized lignin (OL), and the subsequent lignin degradation process in a water-rich environment.

chemical reactions such as the CO_2 reduction reaction,[25,29] C–C bond formation,[30,31] bond scission,[24] and electrochemical transformations.[32,33] Therefore, the use of plasmonic Au photocatalysts, which are eco-friendly and reusable and possess an excellent photostability, is considered to be a potentially effective strategy for transforming lignin derivatives.

Thus, in this study, the photodegradation of lignin model compounds (β-O-4 linkages) is investigated using colloidal Au NPs dispersed in water, as outlined in Fig. 1. Furthermore, non-phenolic lignin model compounds were chosen because they require a higher redox potential compared to phenolic lignin, making them more challenging to degrade. This allows us to evaluate the effectiveness of our strategy for achieving efficient lignin degradation. In addition, the effects of the organic solvent (acetonitrile, MeCN) content of the aqueous system on the photooxidation and degradation behaviors are examined. Furthermore, the driving force for the photooxidation of lignin in a water-rich environment is determined.

Results and discussion

Spherical Au NPs with an average diameter of 13 ± 0.9 nm were employed as plasmonic photocatalysts for the degradation of the synthesized lignin β-O-4 linkage (Fig. S1 and Scheme S1†). Fig. 2a shows the optical characteristics of the reaction mixture before and after the photocatalytic reaction. The intensities of the absorption peaks at 278 and 308 nm increased considerably after irradiation, whereas the localized surface plasmon resonance (LSPR) peak for Au (522 nm) was preserved. The peaks at 278 and 308 nm were therefore attributed to the oxidized form of lignin (Fig. 2a and S2–S4†). A comparative analysis of lignin conversion efficiency was then conducted under various reaction conditions; the results are presented in Table S1.† In the presence of Au NPs and light, lignin photooxidation conversion reached 96.2% after 24 h of light irradiation (Table S1, entry 1 and Fig. S5(a)†). To validate the impact of the Au NPs and light on lignin photooxidation, control experiments were conducted in the absence of light and without the Au NPs (Table S1, entries 2 and 3†). Consequently, a yield of 8% was obtained in the absence of light (Fig. S5(b)†), and no product was detected without the Au NPs (Fig. S5(c)†), demonstrating that both components are required for the reaction to proceed. Furthermore, in the absence of O_2, the conversion was <2% (Table S1, entry 4 and Fig. S5(d)†), confirming that O_2 is required to facilitate lignin photooxidation.
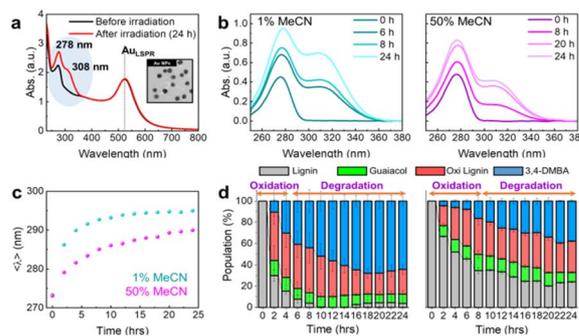

Fig. 2 (a) UV-vis spectra of before (black) and after (red) the photocatalytic lignin photooxidation reaction. The Au LSPR is indicated as a vertical dotted line, showing the stability after irradiation. The inset shows a representative TEM image of the synthesized Au NPs. (b) Transient UV-vis spectra during the photooxidation in 1% MeCN (left) and 50% MeCN (right) in water. (c) Initial moments in the lignin electronic transition as a function of the reaction time (violet: 1% MeCN, magenta: 50% MeCN). (d) Relative populations of normal lignin (NL, gray), oxidized lignin (oxi lignin, OL, red), guaiacol (green), and 3,4-dimethoxybenzaldehyde (3,4-DMBA, light blue) with the corresponding error bars.

As presented in Fig. S6, S7(a), and (b),† four species were directly quantified in the ultraviolet-visible (UV-vis) spectra, namely, normal lignin (NL), oxidized lignin (OL), guaiacol, and 3,4-dimethoxybenzaldehyde (3,4-DMBA), wherein the basis spectra demonstrated doublet features. In addition, Fig. 2b displays the changes in the line shapes, which represent the $\pi \rightarrow \pi^*$ and $n \rightarrow \pi^*$ transitions of the electronic structures.[15] Notably, the peaks observed at 278 and 308 nm increase significantly in intensity during photooxidation in a water-rich environment containing 1% acetonitrile (MeCN, *c.f.*, a 50% MeCN solution). As shown in Fig. 2c, the initial time-dependent changes reveal a convex trend, with red-shifted electronic transitions of the conjugated bonds being associated with the oxidation reaction (Fig. S7(c)†). The evaluation of the 308/278 nm absorbance ratio as a function of time indicates that the reaction proceeded effectively (Fig. S7(d)†), generating abundant photooxidized and lignin degradation products.

The basis spectra of the four components mentioned above facilitated the development of a protocol for quantifying their relative populations (Fig. S8–S10 and Tables S2–S4†). All basis spectra exhibit two main peaks; therefore, two Gaussian profiles were used to determine the reference parameters of these spectra. As the photocatalytic reaction progressed, the transient signals of the four components gradually changed. These spectra were fit to the sum of four sets of two Gaussian profiles as described by eqn (S1), and ensemble populations were extracted from the integrated area of each Gaussian function. Specific details regarding this protocol are provided in the ESI.† However, it is noted that the fitting algorithm commenced using reference parameters derived from the basis spectra, and various criteria being used to apply the fitting constraints. For instance, considering that the ratio between two Gaussian peaks can be used as a fixed parameter, the initial values for fitting the time-dependent spectra were determined from the

fitting results of the previous spectrum. Fitting parameters were also derived from random amplitudes and peak widths within each parameter window, performed over 50 independent fits. The quality of the best fit was verified by comparing the spectra and fits and second derivatives of the spectra (Fig. S8–S10†). The fitting parameters are presented in Tables S2–S4.† Fig. 2d shows the population ensembles as a function of the reaction time under different solvent conditions, *i.e.*, 1 and 50% MeCN (see Fig. S11† for 25% MeCN). Two distinct time regimes are observed. First, the "oxidation dominant" regime exhibits a steep initial rise in the water-rich environment (left plot Fig. 2d) in relation to that observed in the 50% MeCN solution (right plot, Fig. 2d). Second, in the "degradation dominant" regime, the time-dependent variations in the degradation product populations vary significantly between the water-rich and 50% MeCN solutions. This can be accounted for by considering that a water-rich environment may promote lignin degradation by enhancing the photooxidation reaction, which can be inhibited by the presence of MeCN.

To investigate the photocatalytic reaction mechanism, the increasing levels of the oxidation product were monitored over time from the onset of irradiation. The time-dependent curve representing the oxidation reaction is presented in Fig. 3a, along with the calculated reaction rate. Benzoquinone and hydroquinone were used as scavengers for $O_2^{\bullet-}$ to confirm the generation of OL by these species. Notably, the progression of the photocatalytic reaction led to the gradual formation of OL until the $O_2^{\bullet-}$ scavengers were introduced, at which point the production of OL reached a plateau (Fig. 3a). The initial reaction rate (k_1, 5.47×10^{-9} M s^{-1}) decreased upon the addition of the $O_2^{\bullet-}$ scavengers (k_2), reaching 4.76×10^{-10} M s^{-1}, which is approximately 10 times lower. A schematic showing the influence of the $O_2^{\bullet-}$ scavengers is given in Fig. 3b. Based on the obtained results, it was proposed that upon visible light excitation, excited electrons from the Au NPs were transferred to the dissolved O_2 molecules in the reaction mixture, generating highly reactive $O_2^{\bullet-}$ species. These reactive radicals initially reacted with NL, causing photooxidation. However, the scavengers quickly captured the $O_2^{\bullet-}$ species, thereby hindering the formation of OL. The results of kinetic analyses support this proposed mechanism. Subsequently, a range of simple compounds containing benzylic and aliphatic alcohol moieties (see Fig. 4a and S12†) were evaluated to validate the chemoselective photooxidation reaction. It was found that *p*-substituted secondary benzylic alcohol compounds underwent
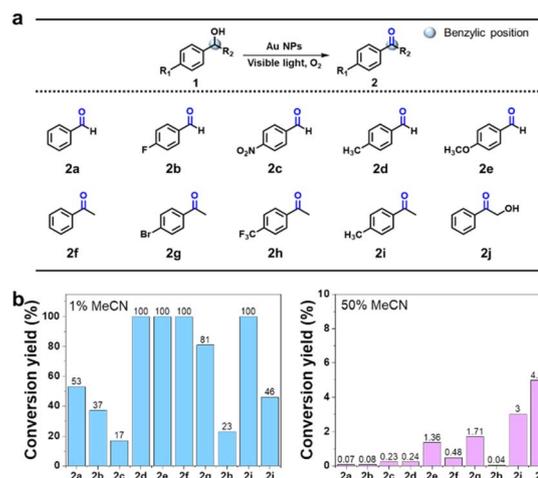
Fig. 4 (a) Au-catalyzed chemoselective photooxidation of the hydroxyl group at the benzylic position. (b) Chemoselective photooxidation yields determined for the compounds shown in panel (a) under different solvent conditions (left: water-rich, right: MeCN-rich).

oxidation regardless of the presence of electron-donating groups or electron-withdrawing groups as substituents (Fig. 4a and S13–S22†). In contrast, primary alcohols rarely underwent photooxidation (Fig. S23–S26†). Following the photooxidation reaction of benzylic alcohol, a peak corresponding to the C=O stretching vibration appeared at ~1700 cm^{-1} in the FT-IR spectrum, whereas this peak was not observed for aliphatic alcohols (Fig. S27†). This assessment was in good agreement with the results of lignin photooxidation at the benzylic position, indicating that chemoselective photooxidation had proceeded successfully. This was attributed to the lower dissociation energy of the benzylic C–H bond than those of aliphatic hydrocarbons, leading to facile hydrogen atom abstraction and the formation of relatively stable radical intermediates.[34,35] Thus, photooxidation at the benzylic position is favorable. Furthermore, the photooxidation yields were examined relative to the solvent conditions (Fig. 4b). Under water-rich conditions, the conversion yields ranged from 17 to 100% (Fig. 4b, left panel). In contrast, model compounds exposed to MeCN-rich conditions exhibited extremely low conversion yields, typically below a few percent (Fig. 4b, right panel). It was therefore proposed that a higher water content leads to the facile disproportionation of $O_2^{\bullet-}$ with the hydrogen atom at the benzylic position in the β-O-4 linkage (see below eqn (2)), producing the hydroperoxide anion (HO_2^-). This reactive species promotes deprotonation at the C_α–OH position, generating OL, as detailed below.

$$AuNPs + h\nu \rightarrow e_{Au}^- + h_{Au}^+ \quad (1)$$

$$O_2 + e_{Au}^- \rightarrow O_2^{\bullet-} \quad (2)$$

$$O_2^{\bullet-} + CH_{C_\alpha,lignin} \rightarrow HO_2^{\bullet} + C_{C_\alpha,hydroxyl}^{\bullet} \quad (3)$$

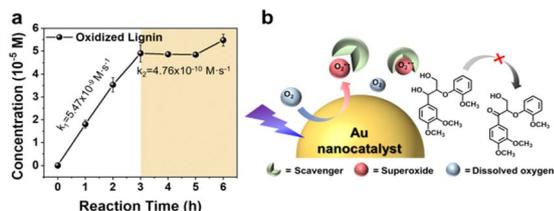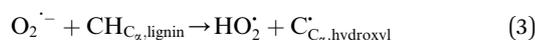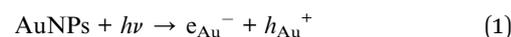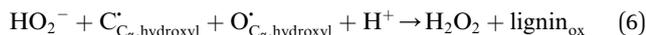$$HO_2^{\bullet} + O_2^{\bullet-} \rightarrow O_2 + HO_2^- \quad (4)$$

Fig. 3 (a) Effect of superoxide ion scavengers on the reaction. (b) Schematic showing of the role of superoxide ion scavengers.

$$h_{\mathrm{Au}}{}^{+} + \mathrm{OH}_{\mathrm{C}_\alpha,\mathrm{hydroxyl}} \rightarrow \mathrm{O}^{\cdot}{}_{\mathrm{C}_\alpha,\mathrm{hydroxyl}} \qquad (5)$$

$$\mathrm{HO}_2{}^{-} + \mathrm{C}^{\cdot}{}_{\mathrm{C}_\alpha,\mathrm{hydroxyl}} + \mathrm{O}^{\cdot}{}_{\mathrm{C}_\alpha,\mathrm{hydroxyl}} + \mathrm{H}^{+} \rightarrow \mathrm{H}_2\mathrm{O}_2 + \mathrm{lignin}_{\mathrm{ox}} \qquad (6)$$

Conversely, under relatively high MeCN conditions, the disproportionation of $\mathrm{O}_2{}^{\cdot-}$ is suppressed. As a result, hydrogen atom abstraction occurs infrequently, thereby limiting oxidation events.

To establish a structural and energetic basis for interpreting the photooxidation reaction results, quantum mechanical calculations were performed using the Hartree–Fock (HF) and density functional theory (DFT) methods at the HF/6-311+G**, B3LYP/6-311+G**, and B3LYP/6-311G** levels of the Gaussian 16 package.[36] A total of 36 different conformational isomers were considered as the initial guesses for the NL and OL species to determine the optimal geometry of the β-O-4-type lignin (Fig. S28 and S29†). The relative single-point energy of a conformational isomer, ΔE, is defined as the energy difference between the isomer (E_i) and the globally optimized "minimum" conformation ($E_{\min}$; Fig. S30, Tables S5 and S6†). As these calculations are performed for molecules in the absence of a solvent, the resulting optimal geometries may not be realistic. Thus, to address this issue, energies (E_i) in isolated and aqueous environments were refined using the self-consistent reaction field (SCRF) method.[37] The geometries of the five key conformations were denoted as "minimum" NL and OL, "flipped" NL and OL, and "twisted" NL, as presented in Fig. S27 and S28.†

Due to the energetic similarities between the two conformers, the optimal structure of OL can adopt both the "minimum" and "flipped" conformations (see the Computational details section and Fig. S30 in the ESI†).

Based on the agreement between the HF and DFT methods shown in Fig. S31,† calculations at the B3LYP/6-311G** level of theory were performed to investigate the electrostatic potential and electron density distributions. It was found that, the molecular electrostatic potentials (MEPs) of NL and OL revealed negative and positive electrostatic potentials localized on the oxygen and hydrogen atoms, respectively, because these are neutral compounds (Fig. S32†). The MEP map of NL is consistent with the previously reported DFT results for a similar lignin compound.[38] It was deduced that the solvation effect increased the overall polarities of NL and OL, suggesting an enhanced ability for both hydrogen bond donation and acceptance. In addition, the highest occupied molecular orbital (HOMO), lowest unoccupied molecular orbital (LUMO), and HOMO–LUMO gaps were calculated to elucidate the chemical stabilities of NL and OL under different solvation states (Fig. S33, S34 and Table S7†). Interestingly, in both the "minimum" and "flipped" forms, the electron densities transferred from one aromatic ring to another when transitioning from the HOMO to LUMO states. Furthermore, solvation induced a red shift in the OL band gap, whereas NL exhibited a blue shift, as shown in Table S7.†

The cleavage of lignin can be initiated at the C_α–C_β bond or C_β–O bond.[39–44] Thus, to elucidate the mechanism of selective C_α–C_β bond cleavage, DFT calculations were performed to
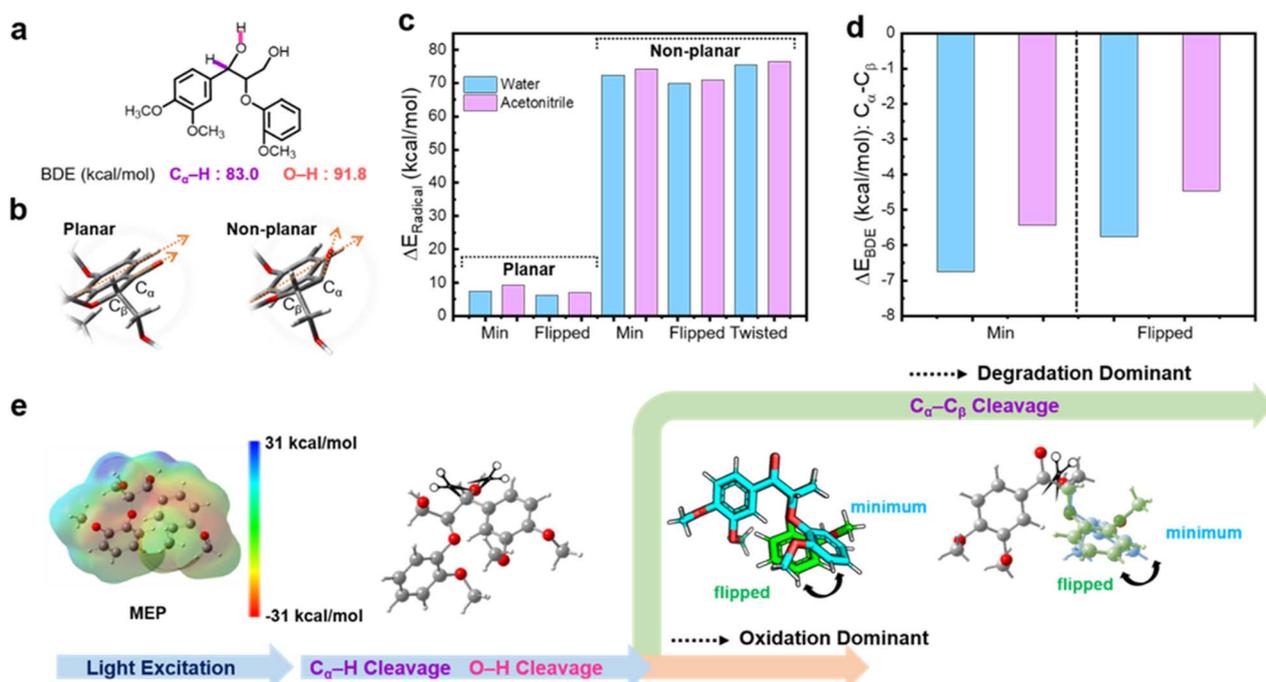

Fig. 5 (a) Bond dissociation energies (BDEs) of the C_α–H and O–H bonds. (b) Orientations of the C_α–O bonds in the planar and non-planar directions. (c) Stabilization energies of radicalized lignin with different structures and orientations. The solvation environments are indicated by different colors. (d) BDEs of the C_α–C_β bonds across varying configurations. (e) Oxidation–degradation kinetics diagram for β-O-4-type lignin, based on kinetic and structural analyses, showing the molecular electrostatic potential (MEP) map (left), C_α–H and O–H cleavage sites, and stable product conformations in the "oxidation dominant" and "degradation dominant" regimes.

Table 1 Stabilization energies of radicalization and C_α–C_β cleavage for the conformational isomers of lignin at the B3LYP/6-311G** level of theory. The minimum, flipped, and twisted conformations are indicated by subscripts "min," "flip," and "twist" labels, respectively. The solvation environment is also indicated

Radicalization (kcal mol^{-1})	Water	Acetonitrile
$\Delta E_{\text{Radical,min}}$ (planar)	7.5	9.2
$\Delta E_{\text{Radical,flip}}$ (planar)	6.2	7.1
$\Delta E_{\text{Radical,min}}$ (non-planar)	72.4	74.2
$\Delta E_{\text{Radical,flip}}$ (non-planar)	75.5	76.4
$\Delta E_{\text{Radical,twist}}$ (non-planar)	70.0	71.0

$\Delta E_{\text{C–C}}$ (kcal mol^{-1})	Water	Acetonitrile
$\Delta E_{\text{C–C,min}}$	−6.7	−5.4
$\Delta E_{\text{C–C,flip}}$	−5.8	−4.5

determine the energetic gains. As shown in Table S8,† the high BDEs of the C_α–C_β and C_β–O linkages (*i.e.*, 50–90 kcal mol^{-1}) typically present a challenge in initiating cleavage.[11,45] In the current strategy, the creation of oxygen radicals activates the O–H bond, which promotes C_α–C_β linkage cleavage. As shown in Fig. 5a, the BDEs of the C_α–H and O–H bonds in neutral NL are relatively high, reaching 83.0 and 91.8 kcal mol^{-1}, respectively.

Interestingly, the oxygen radical can stabilize the radicalization of lignin when the C_α–O bond is oriented in a planar direction, as shown in Fig. 5b and c. These observations indicate that stabilization could be achieved through conformational preferences. Moreover, lignin with a radical character can effectively benefit from energetic advantages of 4–7 kcal mol^{-1} (Fig. 5d and Table 1). Thus, based on the stabilization effect, the mechanistic features of the time-dependent photooxidation reaction can be described. Consistent with the UV-vis population analysis, two time-dependent regimes were observed, namely, the "oxidation dominant" regime (early stage, wherein the "minimum" and "flipped" conformational isomers of OL remain interchangeable, with a low energy difference of 0.4 kcal mol^{-1} between the two isomers), and the "degradation dominant" regime (which indicates energetic advantages for the C_α–C_β linkage, particularly under aqueous conditions).

Conclusions

In conclusion, the photooxidation and degradation of lignin model compounds was demonstrated using a plasmonic Au nanocatalyst in an aqueous environment. Based on the time-dependent spectral changes and structural data, a stepwise mechanism was proposed for the photo-triggered reactions, involving electron transfer, hydrogen abstraction, and degradation. More specifically, electrons in the Au NPs are excited by visible light, and $O_2{}^{\bullet-}$ is generated through the single-electron transfer process. In a water-rich environment, these reactive oxygen species abstract a hydrogen atom from the benzylic carbon of the NL model compound to form a ketone. The photooxidized state of lignin is stabilized in bulk water by an

equilibrium between the "minimum" and "flipped" conformations. Once photooxidation occurs at the benzylic carbon, the C_α–C_β and C–O bonds in the NL lignin become unstable, leading to their cleavage and the formation of two distinct subunits. This photoreaction system is unique because it employs a single-component catalyst in an aqueous medium, distinguishing it from previous studies that utilize organic-based catalysts in organic media.[46–52] Moreover, the chemoselective photooxidation of the benzylic hydroxyl group was achieved in various compounds, contrasting with existing studies that utilized multicomponent heterogeneous catalysts or high temperatures.[53–55] Notably, this photooxidation system opens up new possibilities owing to the use of a single-component catalyst without toxic chemicals or harsh reaction conditions. Overall, these findings provide molecular insights into plasmon-driven chemoselective photooxidation in aqueous environments, emphasizing the significance of understanding the molecular basis of selective oxidization. It is anticipated that these findings will shed light on the impact of the photooxidative reaction solvent on the structure, dynamics, and stability of biomass.

Lignin, a biomass-derived material abundantly available from sources such as wood and agricultural residues, has attracted increasing attention as a promising renewable feedstock for the sustainable chemical industry. To enable its practical utilization, it is essential to address key factors such as process stability and reproducibility, along with the reusability and long-term durability of catalytic systems. With continued advancements in these areas, lignin degradation technologies hold significant potential for industrial-scale applications in biorefineries, green chemical synthesis, and energy-related conversion processes.

Data availability

All data can be obtained from the corresponding authors upon request.

Author contributions

Juhee Ha: writing – original draft, formal analysis, data curation. Jiwon Kang: writing – original draft, formal analysis, data curation. Suk Hyun Lim: data curation. Dae Won Cho: visualization, data curation. Kwang-Im Oh: writing – review & editing, supervision, resources, formal analysis. Youngsoo Kim: writing – review & editing, supervision, resources, formal analysis.

Conflicts of interest

There are no conflicts to declare.

Acknowledgements

Notes and references

1 I. Bosque, G. Magallanes, M. Rigoulet, M. D. Kärkäs and C. R. J. Stephenson, *ACS Cent. Sci.*, 2017, **3**, 621–628.

2 N. Srisasiwimon, S. Chuangchote, N. Laosiripojana and T. Sagawa, *ACS Sustainable Chem. Eng.*, 2018, **6**, 13968–13976.

3 E. Subbotina, T. Rukkijakan, M. D. Marquez-Medina, X. Yu, M. Johnsson and J. S. M. Samec, *Nat. Chem.*, 2021, **13**, 1118–1125.

4 A. Rahimi, A. Azarpira, H. Kim, J. Ralph and S. S. Stahl, *J. Am. Chem. Soc.*, 2013, **135**, 6415–6418.

5 S. Dabral, H. Wotruba, J. G. Hernández and C. Bolm, *ACS Sustainable Chem. Eng.*, 2018, **6**, 3242–3254.

6 J. Chen, W. Liu, Z. Song, H. Wang and Y. Xie, *Bioenergy Res.*, 2018, **11**, 166–173.

7 M. Ko, L. T. M. Pham, Y. J. Sa, J. Woo, T. V. T. Nguyen, J. H. Kim, D. Oh, P. Sharma, J. Ryu, T. J. Shin, S. H. Joo, Y. H. Kim and J. W. Jang, *Nat. Commun.*, 2019, **10**, 1–10.

8 J. D. Nguyen, B. S. Matsuura and C. R. J. Stephenson, *J. Am. Chem. Soc.*, 2014, **136**, 1218–1221.

9 Y. Cao, N. Wang, X. He, H. R. Li and L. N. He, *ACS Sustainable Chem. Eng.*, 2018, **6**, 15032–15039.

10 S. Li, Z. J. Li, H. Yu, M. R. Sytu, Y. Wang, D. Beeri, W. Zheng, B. D. Sherman, C. G. Yoo and G. Leem, *ACS Energy Lett.*, 2020, **5**, 777–784.

11 S. Kim, S. C. Chmely, M. R. Nimlos, Y. J. Bomble, T. D. Foust, R. S. Paton and G. T. Beckham, *J. Phys. Chem. Lett.*, 2011, **2**, 2846–2852.

12 S. H. Lim, H. Jang, M. J. Kim, K. R. Wee, D. H. Lim, Y. I. Kim and D. W. Cho, *J. Org. Chem.*, 2022, **87**, 2289–2300.

13 J. Zakzeski, P. C. A. Bruijnincx, A. L. Jongerius and B. M. Weckhuysen, *Chem. Rev.*, 2010, **110**, 3552–3599.

14 R. Behling, S. Valange and G. Chatel, *Green Chem.*, 2016, **18**, 1839–1854.

15 W. Schutyser, T. Renders, S. Van Den Bosch, S. F. Koelewijn, G. T. Beckham and B. F. Sels, *Chem. Soc. Rev.*, 2018, **47**, 852–908.

16 J. Luo, X. Zhang, J. Lu and J. Zhang, *ACS Catal.*, 2017, **7**, 5062–5070.

17 Z. Xiang, W. Han, J. Deng, W. Zhu, Y. Zhang and H. Wang, *ChemSusChem*, 2020, **13**, 4199–4213.

18 S. Gazi, W. K. Hung Ng, R. Ganguly, A. M. Putra Moeljadi, H. Hirao and H. S. Soo, *Chem. Sci.*, 2015, **6**, 7130–7142.

19 N. Luo, M. Wang, H. Li, J. Zhang, H. Liu and F. Wang, *ACS Catal.*, 2016, **6**, 7716–7721.

20 Y. Liu, C. Li, W. Miao, W. Tang, D. Xue, C. Li, B. Zhang, J. Xiao, A. Wang, T. Zhang and C. Wang, *ACS Catal.*, 2019, **9**, 4441–4447.

21 P. Christopher, H. Xin and S. Linic, *Nat. Chem.*, 2011, **3**, 467–472.

22 S. Linic, P. Christopher and D. B. Ingram, *Nat. Mater.*, 2011, **10**, 911–921.

23 P. Christopher, H. Xin, A. Marimuthu and S. Linic, *Nat. Mater.*, 2012, **11**, 1044–1050.

24 S. Mukherjee, F. Libisch, N. Large, O. Neumann, L. V. Brown, J. Cheng, B. Lassiter, E. A. Carter, P. Nordlander, N. J. Halas, J. B. Lassiter, E. A. Carter, P. Nordlander and N. J. Halas, *Nano Lett.*, 2013, **13**, 240–247.

25 S. Yu, A. J. Wilson, J. Heo and P. K. Jain, *Nano Lett.*, 2018, **18**, 2189–2194.

26 Y. Kim, D. Dumett Torres and P. K. Jain, *Nano Lett.*, 2016, **16**, 3399–3407.

27 Y. Kim, A. J. Wilson and P. K. Jain, *ACS Catal.*, 2017, **7**, 4360–4365.

28 Y. Kim, J. G. Smith and P. K. Jain, *Nat. Chem.*, 2018, **10**, 763–769.

29 S. Yu and P. K. Jain, *Nat. Commun.*, 2019, **10**, 1–7.

30 J. Kim, J. Lee, H. Choi, J. Ha, M. Cheon, Y. Seo, Y. Kim and D. Yoo, *Nanoscale*, 2023, **15**, 15950–15955.

31 J. Lee, P. B. Joshi, A. J. Wilson and Y. Kim, *J. Phys. Chem. C*, 2023, **127**, 8096–8103.

32 Y. Zhang, W. Guo, Y. Zhang and W. D. Wei, *Adv. Mater.*, 2021, **33**, 1–16.

33 E. Contreras, R. Nixon, C. Litts, W. Zhang, F. M. Alcorn and P. K. Jain, *J. Am. Chem. Soc.*, 2022, **144**, 10743–10751.

34 H. Wakefield IV, Q. Jiang and R. S. Klausen, *Org. Biomol. Chem.*, 2022, **20**, 1407–1414.

35 D. Griller and K. U. Ingold, *Acc. Chem. Res.*, 1976, **9**, 13–19.

36 M. J. Frisch, G. W. Trucks, H. B. Schlegel, G. E. Scuseria, M. A. Robb, J. R. Cheeseman, G. Scalmani, V. Barone, G. A. Petersson, H. Nakatsuji, X. Li, M. Caricato, A. V. Marenich, J. Bloino, B. G. Janesko, R. Gomperts, B. Mennucci, H. P. Hratchian, J. V. Ortiz, A. F. Izmaylov, J. L. Sonnenberg, D. Williams-Young, F. Ding, F. Lipparini, F. Egidi, J. Goings, B. Peng, A. Petrone, T. Henderson, D. Ranasinghe, V. G. Zakrzewski, J. Gao, N. Rega, G. Zheng, W. Liang, M. Hada, M. Ehara, K. Toyota, R. Fukuda, J. Hasegawa, M. Ishida, T. Nakajima, Y. Honda, O. Kitao, H. Nakai, T. Vreven, K. Throssell, J. A. Montgomery Jr, J. E. Peralta, F. Ogliaro, M. J. Bearpark, J. J. Heyd, E. N. Brothers, K. N. Kudin, V. N. Staroverov, T. A. Keith, R. Kobayashi, J. Normand, K. Raghavachari, A. P. Rendell, J. C. Burant, S. S. Iyengar, J. Tomasi, M. Cossi, J. M. Millam, M. Klene, C. Adamo, R. Cammi, J. W. Ochterski, R. L. Martin, K. Morokuma, O. Farkas, J. B. Foresman and D. J. Fox, *Gaussian 16 Rev. C.01*, Gaussian, Inc., Wallingford, CT, 2016.

37 R. Ditchfield, W. J. Hehre and J. A. Pople, *J. Chem. Phys.*, 1971, **54**, 720–723.

38 Y. Zhang, H. He, K. Dong, M. Fan and S. Zhang, *RSC Adv.*, 2017, **7**, 12670–12681.

39 L. Jiang, G. Xu and Y. Fu, *ACS Catal.*, 2022, **12**, 9473–9485.

40 M.-W. Zheng, Y. Lang, X. Han, L. Jia, H. Zeng and C.-J. Li, *Cell Rep. Phys. Sci.*, 2024, 102009, DOI: **10.1016/j.xcrp.2024.102009**.

41 Y. Kang, X. Yao, Y. Yang, J. Xu, J. Xin, Q. Zhou, M. Li, X. Lu and S. Zhang, *Green Chem.*, 2021, **23**, 5524–5534.

42 Y. Li, J. Wen, S. Wu, S. Luo, C. Ma, S. Li, Z. Chen, S. Liu and B. Tian, *Org. Lett.*, 2024, **26**, 1218–1223.

43 X. Wu, X. Fan, S. Xie, J. Lin, J. Cheng, Q. Zhang, L. Chen and Y. Wang, *Nat. Catal.*, 2018, **1**, 772–780.

44 H. Liu, H. Li, N. Luo and F. Wang, *ACS Catal.*, 2020, **10**, 632–643.

45 R. Parthasarathi, R. A. Romero, A. Redondo and S. Gnanakaran, *J. Phys. Chem. Lett.*, 2011, **2**, 2660–2666.

46 D. W. Cho, R. Parthasarathi, A. S. Pimentel, G. D. Maestas, H. J. Park, U. C. Yoon, D. Dunaway-Mariano, S. Gnanakaran, P. Langan and P. S. Mariano, *J. Org. Chem.*, 2010, **75**, 6549–6562.

47 R. DiCosimo and H. C. Szabo, *J. Org. Chem.*, 1988, **53**, 1673–1679.

48 S. H. Lim, W. S. Lee, Y. I. Kim, Y. Sohn, D. W. Cho, C. Kim, E. Kim, J. A. Latham, D. Dunaway-Mariano and P. S. Mariano, *Tetrahedron*, 2015, **71**, 4236–4247.

49 D. W. Cho, J. A. Latham, H. J. Park, U. C. Yoon, P. Langan, D. Dunaway-Mariano and P. S. Mariano, *J. Org. Chem.*, 2011, **76**, 2840–2852.

50 P. J. Harvey, H. E. Schoemaker, R. M. Bowen and J. M. Palmer, *FEBS Lett.*, 1985, **183**, 13–16.

51 S. H. Lim, K. Nahm, C. S. Ra, D. W. Cho, U. C. Yoon, J. A. Latham, D. Dunaway-Mariano and P. S. Mariano, *J. Org. Chem.*, 2013, **78**, 9431–9443.

52 V. B. Huynh, *Biochem. Biophys. Res. Commun.*, 1986, **139**, 1104–1110.

53 F. Su, S. C. Mathew, G. Lipner, X. Fu, M. Antonietti, S. Blechert and X. Wang, *J. Am. Chem. Soc.*, 2010, **132**, 16299–16301.

54 Y. Liu, P. Zhang, B. Tian and J. Zhang, *ACS Appl. Mater. Interfaces*, 2015, **7**, 13849–13858.

55 J. L. Dimeglio, A. G. Breuhaus-Alvarez, S. Li and B. M. Bartlett, *ACS Catal.*, 2019, **9**, 5732–5741.